ELSEVIER

Contents lists available at ScienceDirect

# **Applied Thermal Engineering**

journal homepage: www.elsevier.com/locate/apthermeng





# Analysis of time-dependent heat transfer with periodic excitation in microscale systems

Tomer Shockner<sup>a</sup>, Tanvir Ahmed Chowdhury<sup>b</sup>, Shawn A. Putnam<sup>b</sup>, Gennady Ziskind<sup>a,\*</sup>

- <sup>a</sup> Heat Transfer Laboratory. Department of Mechanical Engineering, Ben-Gurion University of the Negey, P.O.B. 653, Beer-Sheva 84105, Israel
- b Department of Mechanical and Aerospace Engineering, University of Central Florida, Orlando, FL 32816, USA

#### ARTICLE INFO

Keywords:
Microscale
Periodic heat transfer
Jet impingement
Local heat flux

#### ABSTRACT

This study investigates time-dependent heat transfer with periodic excitation in micro-scale systems. Specifically, this study sheds light on time and length scales relevant to periodic heat transfer in micro systems. First, a system's substrate is modeled as a slab of finite thickness, in which the heat conduction equation is solved analytically for a periodic temperature boundary condition over the entire range of transient-periodic process. Using the analytical solutions, the system reaction in time is characterized for time scales and material properties typical for micro-systems. A "penetration depth" is defined as a parameter which indicates the maximum distance from the periodically-heated boundary/surface at which the periodic-thermal excitations are still noticeable. Then, as a case study, an experimental device is examined that uses a round, impinging water jet to cool a surface heated by pulsing laser. Finally, a three-dimensional numerical simulation, validated versus experiments, is used to elucidate the system's expected thermal behavior, including spatial and temporal temperature field variation, relevant time scales for measurements, and the spatial distribution of the heat transfer coefficient. It is demonstrated that the analytical findings can serve to characterize the real behavior rather accurately. The findings can assist in the design of systems with unsteady heating, and in future studies aiming at understanding more complex physically-driven transient phenomena, like flow boiling in micro-systems.

#### 1. Introduction

Heat removal in micro-electronic devices is currently a major challenge that limits their reliability and lifespan. In these systems, power densities have been rising to new heights for which the traditional aircooling heat sinks have reached their limit for high-end applications [1]. For example, the density of transistors in modern chips is so enormous that the thermal power density that needs to be dissipated is above 100 W/cm² and predictions are that soon it will be approaching 300 W/cm² [2]. According to Yarin et al. [1], the maximum heat transfer coefficient of a standard fan is approximately 150 W/m² K; i.e., it can remove about 1 W/cm² for 60 K temperature difference. Therefore, state-of-the-art cooling systems employ smart cooling schemes in order to enhance the heat transfer characteristics of micro-systems.

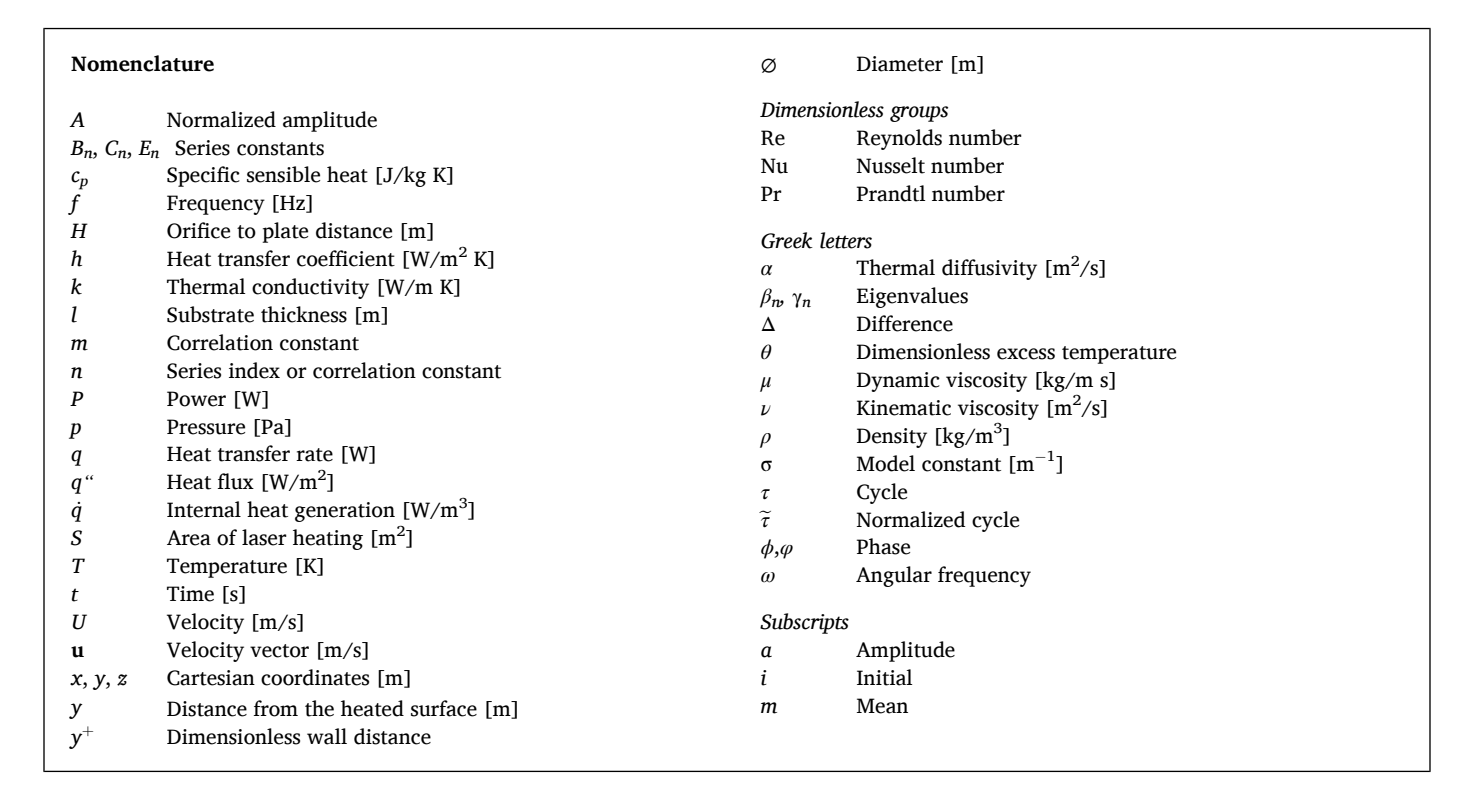
Furthermore, in micro-electronics applications transient thermal behavior with periodic characteristics is quite common, as exemplified in Fig. 1. The temperature fluctuations might result from the electronic component operation regime, which may include temporary power spikes [1], see Fig. 1a. Thermally speaking, this electronic component

acts as the micro-system's variable heat source. Another example is alternation of the heat removal due to oscillating flow-field of a micro jet impingement or in a micro/mini channel [3–10], see Fig. 1b, which can be utilized in order to enhance heat transfer characteristics. In both cases, namely, fluctuating heat generation of the electronic component or intentionally oscillating flow-field of the cooling scheme, the periodicity of temperature or heat flux variation is known a priori, even if their actual values could be estimated only. An even more complex scenario occurs when the oscillations are the result of a physically driven mechanism such as flow boiling [11–17], in which the alternation is caused by the inherent physics of the system – like a passing bubble generated by boiling itself, see Fig. 3b – and not by a known excitation. Below, the details of different existing and emerging relevant processes are presented in some detail.

Micro-channel-based cooling schemes have been extensively studied over the last decades. Their main advantages in microchip cooling applications are a low-height profile, a single inlet/outlet, ease of manufacture and proximity to the heat sources. While their performance is good, some inherent limitations exist. For instance, non-uniform temperature distribution along channel length can affect the performance.

E-mail address: gziskind@bgu.ac.il (G. Ziskind).

<sup>\*</sup> Corresponding author.



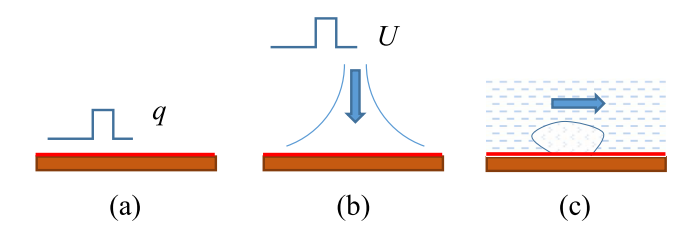


**Fig. 1.** Examples of unsteady behavior: (a) power spike in an electronic component, (b) cooling by a pulsed jet, (c) bubble passing near a cooled surface in flow boiling.

Also, heat transfer may be reduced due to thermal boundary layer buildup. Another way of cooling is based on jets, impinging perpendicular to the heated surface. This method is well known to have superior heat transfer characteristics, but is typically limited to small areas. Also, jet impingement can lead to large thermal gradients over the surface and requires bulkier delivery systems. On the other hand, jet impingement has very impressive performance at micro scale. Recent studies have demonstrated the capabilities of steady micro jets to dissipate heat fluxes in excess of >1 kW/cm<sup>2</sup> with temperature rise of only 27  $^{\circ}\text{C}$  [17–19]. In those investigations, the heat transfer coefficients exceeded 4  $\times$  10<sup>5</sup> W/m<sup>2</sup> K. Some recent studies have shown that at micro-scale the combination of micro-channels and jets is very beneficial to the heat transfer [20-24]. For example, in a detailed study of micro-gap flow enhanced by a slot-type jet, a 4-fold increase was found even in the developing region of the thermal boundary layer, which generally has higher heat transfer [22]. A recent in-depth survey regarding heat transfer in single-phase liquid for steady jet impingement can be found in Ref. [25].

Heat transfer enhancement can be achieved by imposing oscillations on the flow. These oscillations can generate large perturbations that break up and disrupt the growth of the hydrodynamic and thermal boundary layers and, as a result, significantly enhance heat transfer while sustaining low flow rates, as has been shown in a number of

studies. As early as 1961, Nevins and Ball [26] were the first to try a pulsed jet for this purpose, while active studies in the field have continued over the years, see e.g. Refs. [27-31] and also Ref. [32] for a discussion. More recently, Mohammadpour et al. [3] studied the effects of oscillating flow on the heat transfer rate to a slot jet impinging a concave surface. Gitan et al. [4] studied the effect of pulsating twin jets' mixing region on the enhancement of heat transfer. In Ref. [31], a piezoelectric jet, explored experimentally for various Reynolds number and geometrical parameters, revealed an improvement in the areaaveraged Nusselt number of up to 20%, when compared with a steady circular jet. During the last decade, different aspects of cooling by oscillating flows on micro-scale were studied, such as the stagnation point Nusselt number of an axisymmetric impinging synthetic jet [5], the effect of flow pulsation on the local convective heat transfer to an axisymmetric impinging air jet [6], and pulsating flow in a single-phase liquid flow mini-channel [7]. Instead of alternating the flow-field directly, Klein and Hetsroni [8] actuated the target surface of a 2D steady laminar liquid impinging micro-jet. Their findings revealed that the heat transfer coefficient was enhanced by up to 34% in the wall jet region.

Another apparent method to improve heat transfer in micro-channels is the use of boiling, which is expected to allow higher heat transfer coefficients and less pumping power. Because of the small size of the channel, a quasi-periodic behavior would be the result of the inherent physical mechanism - bubble growth and channel cross-section blocking, which can alter the heat transfer coefficient temporarily. Rao et al. [11] conducted experiments using a single microchannel in order to study the transient temperature behavior during several boiling flow patterns: bubbly flow, elongated bubble (slug) flow, partial wall dry-out, and critical heat flux (CHF). During the experiments, synchronized surface temperature and flow regime observation were recorded. In the experiments, intermittent dry-out and re-wetting events with drastic thermal cycling in the measured wall temperature were observed, with characteristic instability frequency of about 25 Hz. The boiling events were modeled as a temporal square-wave function of the heat transfer coefficient via numerical simulations. Bigham and Moghaddam [12] examined heat transfer events in flow boiling in a microchannel,

surveying three different substrate structures for experimental micro systems. Their results revealed that in substrates with high thermal conductivity, such as Silicon ( $k=130~\rm W/m~\rm K$ ), lateral heat conduction was pronounced within the substrate. As for low thermal conductivity substrates, such as Pyrex ( $k=1.2~\rm W/m~K$ ), the dominant heat transfer mechanism was highly dependent on the boundary conditions induced by the flow field. A third option considered was to fabricate a composite substrate consisting of a highly conductive wall, such as silicon, coated with a low thermal conductivity polymer (order of  $10~\rm \mu m$  thickness). This configuration allowed to decouple the heat transfer events especially in boiling heat transfer. There exist other works in which temperature was measured along with synchronized pictures of the flow, and similar periodic behavior was observed, e.g. [13–14].

As conveyed above, periodic thermal changes exist in microscale systems either because of the electronic component nature or in order to increase heat transfer characteristics by advanced cooling schemes. These thermal periodic changes are usually complex, asymmetric and sometimes include sudden jumps in temperature or heat flow. Periodic changes of temperature are also encountered in other, more classical, fields of engineering such as geology; e.g., the periodic heating of the earth's surface during the daily and annual sun cycles. By thermal analysis, one can deduce to which depth these variations cause a noticeable temperature change. Periodic thermal problems are also found in traditional industrial fields, like regenerators of blast furnaces and engine's cylinders. Even though these problems are quite complex, a lot of valuable insight can be gained by approximating the periodic excitation to a simple sinusoidal wave, to which analytical solutions have been derived and can be found in classical heat conduction literature [33-37]. Modern studies can benefit from employing existing analytical solutions to obtain simple relations that help to predict the fundamental features of the system behavior. For instance, Khedari et al. [38] adopted analytical solutions from Carslaw and Jaeger [33] to treat a finite cylinder with periodic boundary conditions over all the surfaces.

This study aims at understanding time-dependent heat transfer in microscale systems with periodic features. The investigation proposes an analytical approach, based on existing conduction heat transfer literature, to derive a solution for a finite slab with unidirectional temperature distribution, subjected to temporal periodic temperature changes. This slab is used to model a micro system's substrate. Then, the analytical solutions are used to perform a parametric study about the penetration depth, a parameter which indicates the distance from the periodic boundary at which the excitation is still noticeable. Obviously, the theory for single-phase heat transfer on micro- and macro-scale is the same. However, the dimensions can be very important for penetration depth: for a large body, a semi-infinite solid approximation may be sufficient, but for a small (thin) one it is not. For this reason, the analysis of microscale transient phenomena should be performed with caution.

The suggested approach is general and not designed for a specific experimental or practical configuration. Still, in order to illustrate the relevance of our analytical tool to more realistic micro systems, an experimental demonstration is performed. The experimental apparatus includes a metal surface on glass which is locally heated by a pulsed laser and is cooled by round, single-phase liquid impinging jet. The periodic temperature changes of the laser-heated surface are characterized by an IR-camera to reveal the spatiotemporal temperature distribution in the stagnation zone. Finally, a 3D numerical simulation is developed and validated with the experimental spatiotemporal temperature distribution data. The numerical tool allows us to explore the real system's substrate temperature behavior, which is then compared with the analytical tool predictions. The correlation between the solution for the analytical unidirectional temperature distribution and the numerical prediction is quite remarkable in regard to the penetration depth.

# 2. Substrate reaction to periodic boundary conditions

As stated above, in practical microscale problems thermal changes

are usually complex, rather than being simply periodic. However, to obtain insight in those complex thermal behaviors, conduction response to a simple sinusoidal excitation should be examined first. A general conduction problem can be classified with respect to its spatial coordinates (as lumped of distributed) and temporal dependence (as transient or periodic) [35]. An unsteady-periodic problem is comprised of transient-periodic, also referred to as starting periodic [35], and steady-periodic intervals. A semi-infinite body with periodic temperature boundary condition has a well-known solution for steady-periodic state [33–37]. However, it is shown below that a micro-system substrate usually cannot be described as a semi-infinite body.

Therefore, a 2D substrate of finite thickness, l, which is subjected to simple periodic changes, has to be modeled. It is assumed that the substrate is comprised of an isotropic material, has no heat generation and has a uniform initial temperature  $T_i$ . To account for the periodic thermal behavior, we dictate a temperature boundary condition on one of the substrate walls as  $T_w(t) = T_m + T_a \sin(\omega t + \varphi)$ , where  $T_m$  is the mean temperature of the oscillatory sine wave,  $T_a$  is the amplitude of the temperature oscillation,  $\omega$  is the angular frequency, and  $\varphi$  is the phase of the temperature wave. Regarding the second boundary, in reality it can be either insulated (though not perfectly) or exposed to the surroundings. For both cases, the amount of heat transfer from this second boundary to the ambient is relatively small. The analytical solutions in the literature, introduced below, treat this opposite boundary as either insulated or assigned with a specific temperature. The latter option would cause the spatial-temporal temperature distribution to be drawn to the prescribed temperature in a way that does not reflect the real situation in micro-scale systems. Thus, only the first model (one boundary periodic, the second boundary insulated) is considered here.

## 2.1. Mathematical modeling

The substrate is modeled as a slab with unidirectional time-dependent temperature distribution. To determine the full thermal behavior analytically, one should solve the general heat conduction equation, if possible, using the appropriate mathematical method. For simplicity, we limit our discussion to time-dependent unidirectional heat conduction problems which are governed by the following partial differential equation:

$$\frac{\partial T}{\partial t} = \alpha \frac{\partial^2 T}{\partial y^2} \tag{1}$$

where T is the temperature of a point y at time t and  $\alpha$  is the material thermal diffusivity. Since the equation is linear, superposition is performed for two existing solutions from the literature [33] in order to build the model. To construct the solution of a slab with a constant initial temperature, having a periodic temperature boundary condition on one side and an insulation boundary condition at the other side, a symmetric slab is considered. This slab has a finite thickness of 2l with the origin of the spatial coordinate y at its center, as illustrated in Fig. 2. The model is comprised of two solutions as described below.

The first solution is of a symmetric slab with uniform initial temperature; this basic solution is used in order to allow the substrate to heat-up from the initial temperature to the periodic mean temperature. The boundary conditions are  $T_w = 0$  at  $y = \pm l$  and the initial condition is  $T_i$ . The solution is [33]:

$$T(y,t) = \frac{4T_i}{\pi} \sum_{n=0}^{\infty} B_n exp(-\alpha \beta_n^2 t) cos(\beta_n y)$$
 (2)

where  $\beta_n$  are eigenvalues and  $B_n$  are series constants defined as:

$$\beta_n = \frac{(2n+1)\pi}{2l} \tag{3}$$

$$B_n = \frac{(-1)^n}{2n+1} \tag{4}$$

The second solution is of a symmetric slab with periodic surface temperature. The symmetric boundary conditions are  $T_w(t) = T_a \sin(\omega t + \varphi)$  at  $y = \pm l$  and the initial condition is zero. The solution is [33]:

$$\frac{T(y,t)}{T_a} = \underbrace{A(y)sin(\omega t + \varphi + \phi(y))}_{steady-periodic solution} + \underbrace{4\pi\alpha \sum_{n=0}^{\infty} C_n exp(-\alpha \beta_n^2 t) cos(\beta_n y)}_{transient solution}$$
(5)

where A(y) is the amplitude,  $\phi(y)$  is the phase delay and  $C_n$  is the series constants, defined as:

$$A(y) = \left| \frac{\cosh(\sigma y(1+i))}{\cosh(\sigma l(1+i))} \right|$$
 (6)

$$\phi(y) = \text{angle}\left(\frac{\cosh(\sigma y(1+i))}{\cosh(\sigma l(1+i))}\right)$$
(7)

$$C_{n} = \frac{(-1)^{n}(2n+1)\left[4l^{2}\omega\cos(\varphi) - \alpha(2n+1)^{2}\pi^{2}\sin(\varphi)\right]}{16l^{4}\omega^{2} + \alpha^{2}\pi^{2}(2n+1)^{4}}$$
(8)

where  $\sigma = (\omega / 2\alpha)^{1/2}$  is a parameter introduced for simplicity.

The first term in Eq. (5) is the steady-periodic solution, whereas the second term is the transient-periodic solution. The amplitude and phase can also be defined as functions of two dimensionless quantities: y/l and  $\sigma l$ , respectively. It is worth mentioning that other advanced textbooks include a solution for the steady-periodic interval (see, e.g., Ref. [34]).

#### 2.2. Analytical solution

The full time-dependent solution of a slab with constant initial temperature, which is insulated from all boundaries, except from one boundary where the temperature is oscillating, is devised in this subsection. The above-mentioned solutions are super-positioned to solve the slab. The conditions used are  $T(\pm l,t) = T_m + T_a \sin(\omega t + \varphi)$ ,  $T(y,0) = T_i$ , see Fig. 2. Since the slab is symmetric, half of it is considered with perfect insulation at y=0. For the sake of superposition, the dimensionless excess temperature  $\theta$  is defined as:  $\theta = (T - T_m) / T_a$ . The new initial and boundary conditions in terms of  $\theta$  are  $\theta(\pm l,t) = \sin(\omega t + \varphi)$ ,  $\theta(y,0) = \theta_i$ . The superposition is  $\theta = \theta_1 + \theta_2$ , where  $\theta_1$  is the slab response to periodic boundary conditions with zero initial condition and  $\theta_2$  is the slab response to zero boundary condition for constant initial temperature. The full solution is:

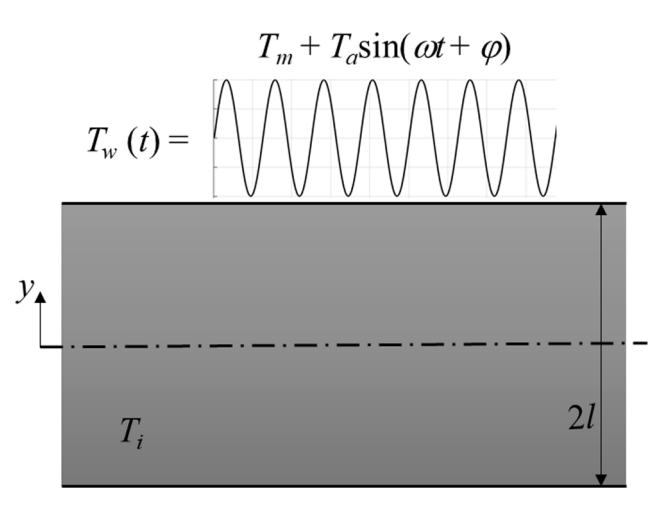


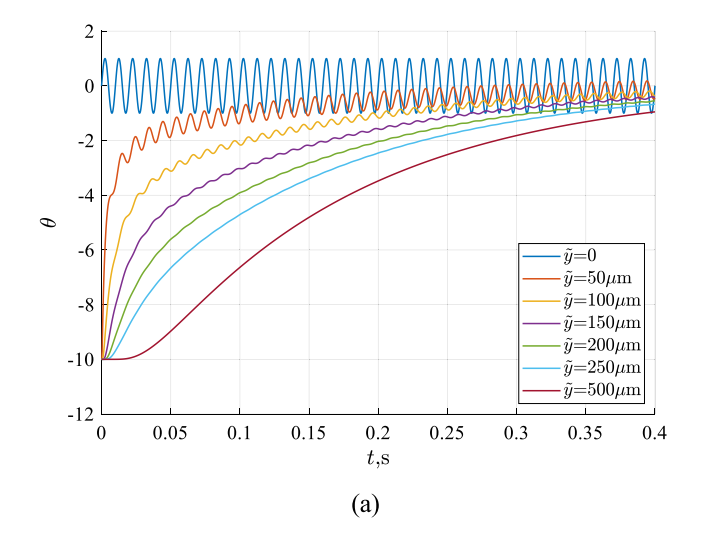
Fig. 2. The schematics of the symmetric slab.

$$\theta(y,t) = \underbrace{A(y)sin(\omega t + \varphi + \phi(y))}_{\theta_1 \text{ steady-periodic solution}} + \underbrace{\frac{4\pi\alpha\sum_{n=0}^{\infty}C_nexp(-\alpha\beta_n^2t)cos(\beta_ny)}{\theta_1 \text{ unsteady-periodic solution}}}_{\theta_1 \text{ unsteady-periodic solution}} + \underbrace{\frac{4\theta_i}{\pi}\sum_{n=0}^{\infty}B_nexp(-\alpha\beta_n^2t)cos(\beta_ny)}_{\theta_1 \text{ solution}}$$
(9)

As shown in Equation (9), this solution may be separated into three parts: unsteady periodic, steady periodic, and the transient behavior in response to the constant boundary condition. The solution is implemented using MATLAB [39]. For each series, 500 terms were calculated, noting that the magnitude of the last term was on the order of  $10^{-7}$ . The time step of  $\Delta t = (50f)^{-1}$  is implemented such that the correct wave behavior in time domain is observed, where f is the frequency of the sinusoidal excitation. In this work, the distance from the periodically-heated boundary (into the Pyrex slab) is referred to as the depth  $(\tilde{y})$  – e.g., for this case,  $\tilde{y} = l - y$ .

# 2.3. Analytical results

For a test case, a substrate made of Pyrex with the following properties:  $\rho=2,230~{\rm kg/m^3},~c_p=750~{\rm J\cdot kg^{-1}\cdot K^{-1}},~k=1.14~{\rm W\cdot m^{-1}\cdot K^{-1}},$  is modeled to be half of the symmetric slab. The substrate is of thickness  $l=500~{\rm \mu m}$  and is exposed to a single sine wave ( $f=100~{\rm Hz},~\phi=0$ ) with an initial temperature difference of 10 °C. The excess dimensionless



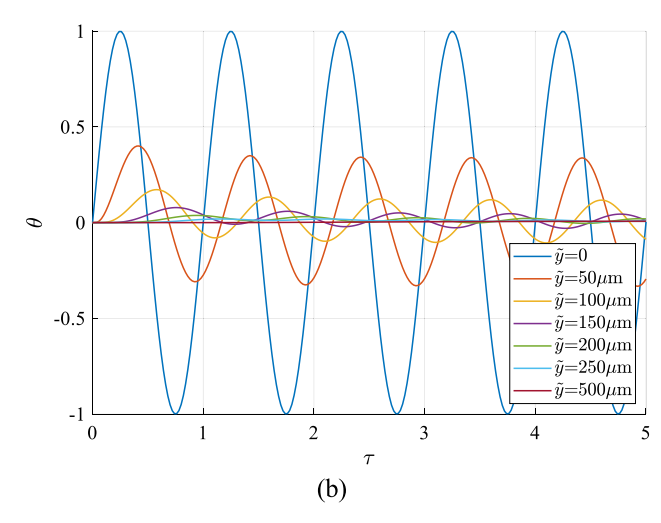


**Fig. 3.** Slab excess temperature for different depths (a) vs. time for full transient-periodic sequence, (b) vs. cycle for unsteady and steady periodic ( $\theta_1$ ).

temperature profile for different depths as a function of time is presented in Fig. 3a. One can see that the temperature rises to match the mean temperature ( $\theta = 0$ ) at all the different depths. Also, there is a growing decay in the amplitude and a delay in the phase as the points are getting deeper into the slab. To observe the periodic behavior more carefully, only the solution of  $\theta_1$  is examined, as illustrated in Fig. 3b. Here, a dimensionless cycle time is used ( $\tau = t \cdot f$ ), such that the number of periods the system undergoes is explicitly shown. Fig. 3 shows that it takes about two periods for the unsteady periodic behavior to decay; i.e., for  $\tau$ > 2, the excess temperature profile (for each depth) seems to be perfectly periodic with respect to itself. In Fig. 3, the boundary excitation  $(\tilde{y} = 0)$  is represented by the blue lines, where the other lines  $(\tilde{y} > 0)$  represent the excess temperatures at different depths into the Pyrex slab. The magnitude of amplitude decay and phase delay for different depths is quite significant. For example, for the depth of 50 µm (10% into the substrate), the amplitude is about 40% of the excitation amplitude, and for the depth of 200  $\mu m$  (40% into the substrate) the amplitude is almost completely damped.

In order to assess quantitatively whether the periodic excitation is felt at certain depth, the "penetration depth" is introduced. This notion is often used in fluid dynamics; for instance, when unsteady unidirectional flow due to an oscillating plane boundary is examined, then the penetration depth defines the thickness of the liquid layer to which the flow-field distribution is effectively confined [40]. This concept can be also applied to transient (non-periodic) conduction. For instance, when a slab at ambient temperature is subjected to uniform heat flux at one wall while the other wall is exposed to ambient, the penetration depth can be defined in an analogous manner to the notion of boundary-layer thickness [35]. In our case, it is defined as the depth where the amplitude magnitude is just 10% of the excitation amplitude. Fig. 4 provides penetration depth data for the studied case. Based on Eq. (1), the amplitude at a certain depth is a function of the following parameters: excitation frequency (f), thermal diffusivity of the substrate material  $(\alpha)$ ,

and substrate's thickness (*l*). For the present case,  $l=500~\mu\text{m}$ , f=100~Hz, and  $\alpha=6.57\times10^{-7}~\text{m}^2/\text{s}$ . As a result, the penetration depth is 105  $\mu\text{m}$ , which means that at depths beyond  $\sim20\%$  of the substrate thickness that the periodic excitation is almost completely dissipated.

The idea of penetration depth may be used also to compare the wellknown solution of semi-infinite body [34] with the solution for a slab of finite thickness (using the same periodic excitation conditions for both cases). Four comparisons are made based on two different materials and two different slab thicknesses ( $l = 50, 500 \mu m$ ), see Fig. 5. The examined materials are typically used for micro-systems fabrication: Pyrex ( $\alpha$  $6.57 \times 10^{-7} \text{ m}^2\text{/s})$  – which represents a low thermal conductivity (electrically insulating) material and Silicon ( $\alpha = 797.410^{-7} \text{ m}^2/\text{s}$ ) – which represents the high thermal conductivity (semi-conductor) used in microelectronics. The comparison reveals two limit cases and two intermediate modes, as presented in Fig. 5. In the first case, with relatively low thermal conductivity and thick substrate, the periodic excitation amplitude diminishes to zero within the finite slab thickness, thus the result coincides with the semi-infinite result, see Fig. 5a. However. with relatively high thermal conductivity and thin substrate, as illustrated in Fig. 5d, it is evident that the semi-infinite plate does not describe the finite slab amplitude behavior at all. As can be seen from Fig. 5b and Fig. 5c, in the intermediate cases there is a growing discrepancy between the two analytical solutions. Thus, it is preferable to use the finite-slab solution in order to avoid significant errors.

To further understand the relations between the penetration depth and each parameter: slab thickness (l), excitation frequency (f), and thermal diffusivity ( $\alpha$ ), we examine the penetration depth profile as a function of each parameter separately, while the other parameters are set constant, according to the studied case above. Fig. 4b demonstrates the relation between the penetration depth and the slab thickness. The penetration depth was calculated and plotted in the figure for slab thicknesses varying from 1  $\mu$ m to 2 mm. The results show that for the slab thickness of up to 136  $\mu$ m, the penetration depth equals to the

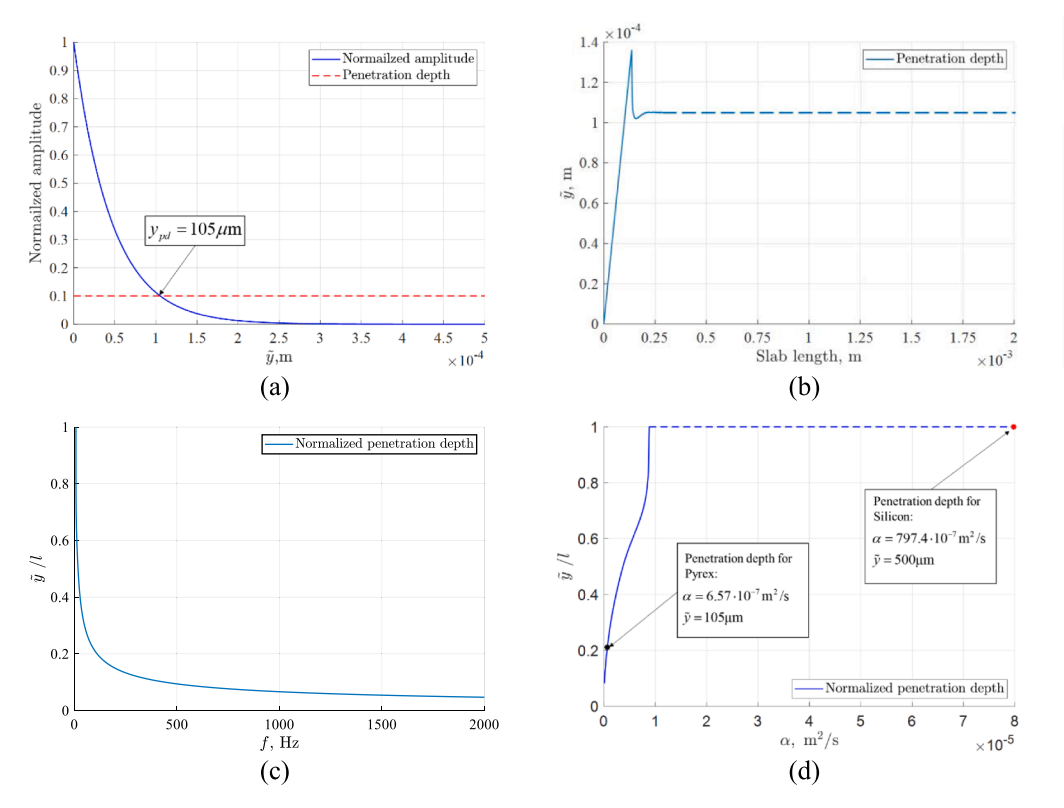


Fig. 4. Analysis of penetration depth: (a) normalized amplitude vs. distance from the slab surface, (b) penetration depth vs. Pyrex slab thickness, (c) normalized penetration depth for a 500  $\mu$ m thick Pyrex slab as a function of the thermal diffusivity.

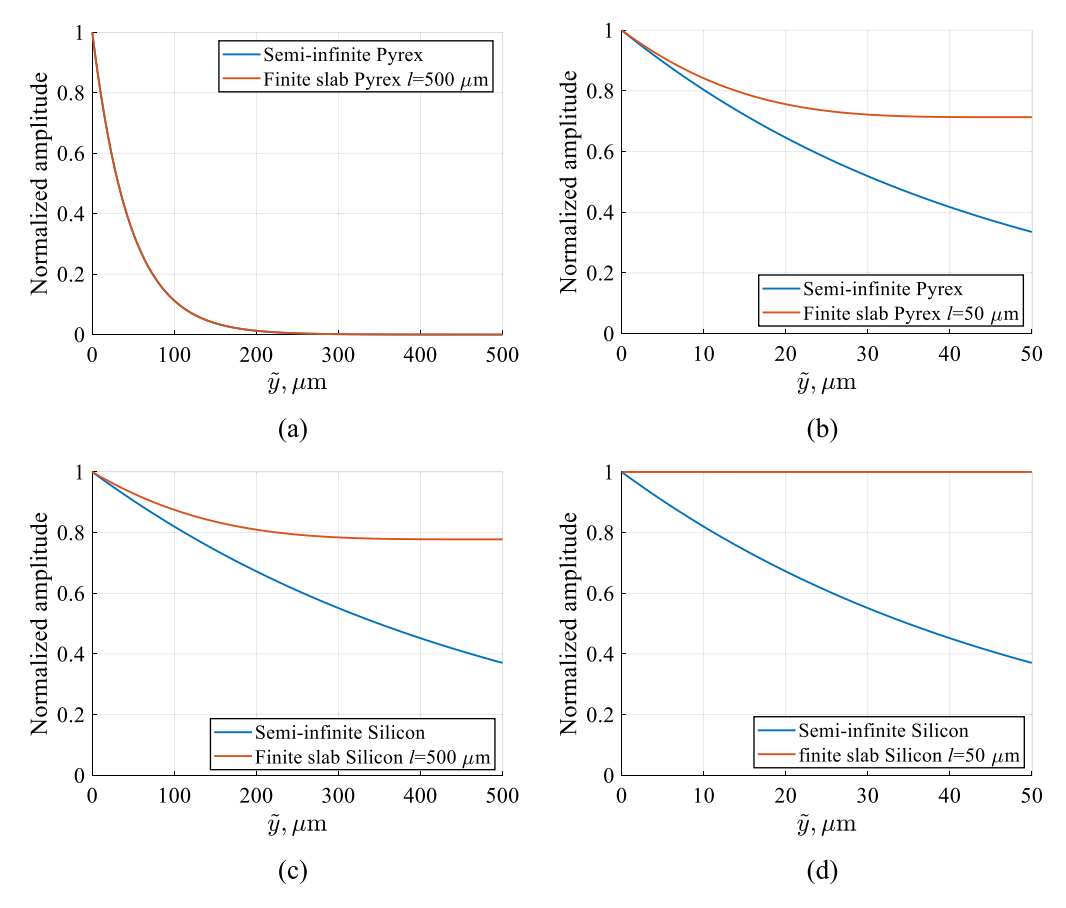


Fig. 5. Comparison of the penetration depth between a semi-infinite plate and a finite slab made of the same material: (a) Pyrex slab of thickness 500 μm, (b) Pyrex slab of thickness 50 μm, (c) Silicon slab of thickness 500 μm, (d) Silicon slab of thickness 50 μm.

thickness, whereas as the slab becomes thicker, the penetration depth is decreasing and for the thickness of 158  $\mu m$  there is a minimum point where the penetration depth equals to 102  $\mu m$ . For l>220  $\mu m$  the penetration depth is about 104  $\mu m$ . This plateau in the penetration depth, the dashed line in Fig. 4b, represents the substrate thickness for which the semi-infinite solution is valid; for cases where the substrate thickness is less than 220  $\mu m$  (the full line in Fig. 4b), the finite slab solution must be used.

The penetration depth versus different frequencies ranging from 10 Hz to 2 kHz is plotted in Fig. 4c. As the frequency increases, the normalized penetration depth decreases in what seems to be  $e^{-af}$  form, where a is greater than zero. This means that for low frequencies the system will demonstrate a strong periodic behavior, whereas for high frequencies it will behave as if there was no periodic excitation at all. The type of material is influencing the penetration depth via the thermal diffusivity. Again, the thermal diffusivities considered are based on the materials used for micro-systems manufacture, ranging from low thermal conductivity materials like Pyrex to high thermal conductivity materials like Silicon. In contrast to Fig. 4b and 4c, in Fig. 4d the normalized penetration depth increases with the increase in the thermal diffusivity: for materials with thermal diffusivity larger than a certain threshold,  $88.2 \times 10^{-7}$  m²/s in the considered case, the relative penetration depth equals unity and is presented in the figure as a dashed line.

# 3. Round jet impingement with pulsing laser heating

In this section, an experimental demonstration of periodic heat transfer is reported. A pulsing laser generates a local hotspot on a surface, which is cooled by a water jet impingement. During the experiments, temperature variations are measured by an IR-camera in order to track the spatiotemporal temperature of the heated wall. A 3D numerical

model is developed in accordance to the experimental system, to characterize the processes in detail. The simulation results are compared to both the experimental data and a heat transfer correlation from the literature [41]. Furthermore, the validated numerical results are compared with the analytical solution for the penetration depth, to demonstrate the applicability of the analysis presented above.

# 3.1. Experimental study

The experimental apparatus is used to capture the temperature distribution at a surface which is heated by localized laser pulses and is cooled by an impinging water jet. Fig. 6 illustrates the experimental submerged jet cooling device. Fig. 6a is a schematic of dual-syringe flow-loop design for this jet cooling device. The closed flow-loop design is aided by a computer-controlled stepper stage, where the double stainless steel piston syringes are connected to each other. A set of four one-way valves are also integrated to the flow-loop system, to facilitate a continuous jet flow which is independent of the stepper-stage pumping direction.

Fig. 6b is a schematic of the submerged jet cooling chamber, using a diode laser for generating a local hotspot and IR thermography for measuring the spatiotemporal temperature. The jet cooling chamber represents a thin-cylindrical geometry and consists of two glass windows sealed with pressure on a Viton O-ring. The O-ring seal is pierced by two syringe needles on opposite sides. The thickness and diameter of the glass windows are  $H=3.175~\mathrm{mm}$  and  $\varnothing=50.8~\mathrm{mm}$ , respectively. The jet inlet window is center drilled for insertion (and subsequent optical adhesive bonding) of a syringe needle with a measured inner diameter of  $\sim 1.2~\mathrm{mm}$ . Thus, a 1.2 mm in diameter de-ionized (DI) water jet is discharged into a thin-cylindrical chamber with the height and diameter of  $H=3.175~\mathrm{mm}$  and  $\varnothing=50.8~\mathrm{mm}$ , respectively. The heat transfer (or

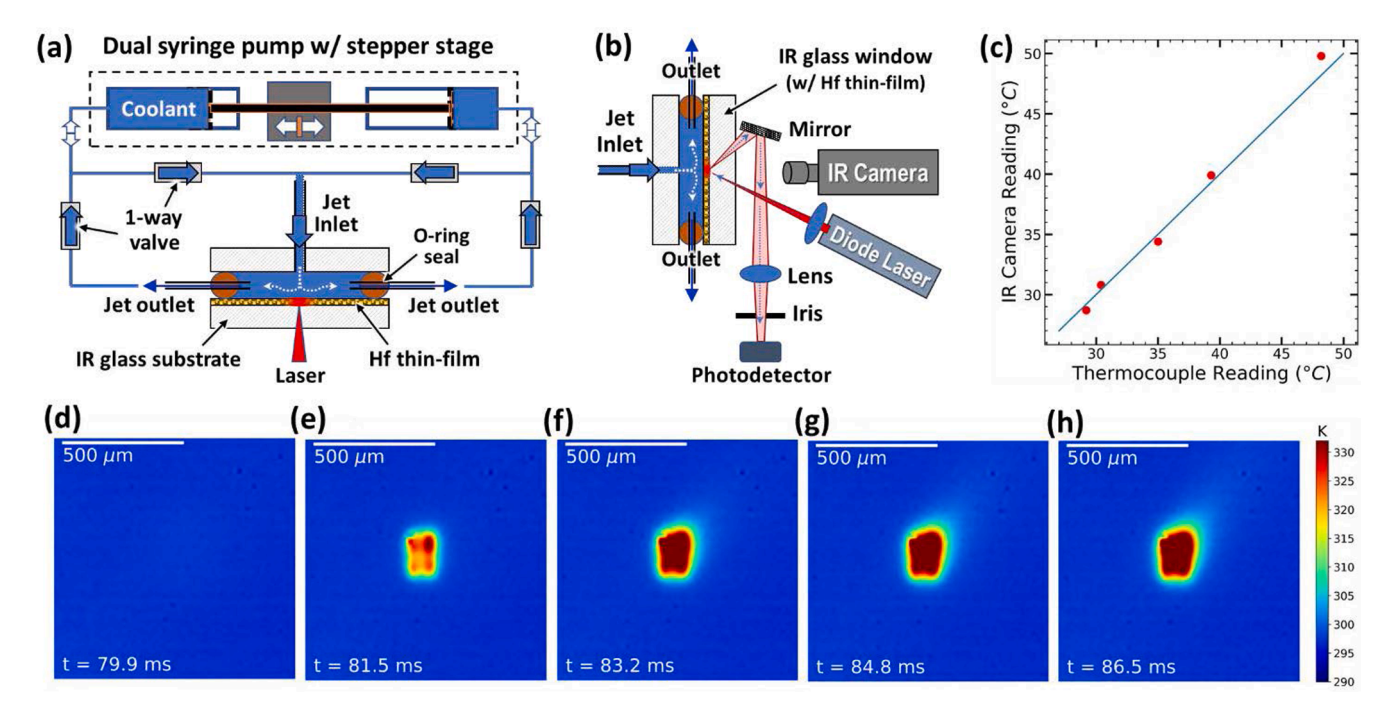


Fig. 6. Experimental jet cooling device and IR thermometry: (a) jet impinging flow loop, (b) submerged impinging jet chamber with the pulsing focused diode laser and IR-thermography, (c) IR camera calibration data, and (d-h) sequence of representative snapshot IR camera images for laser heating at 75 Hz.

impinging jet) window is fabricated from IR-transparent Fused Silica (FS) glass with the same diameter as the channel. The IR-FS window substrate is coated with a 100 nm thick Hafnium (Hf) thin-film via DC magnetron sputtering, where  $\sim 10$  nm of  $HfO_2$  is used as an adhesion layer. As shown in Fig. 6b, the Hf thin-film coating is in direct contact with the submerged DI-water coolant pool.

A focused diode laser of blue light (445 nm) is used as the heating source. The diode laser is incident to the back-side of the IR-FS impinging jet window. As illustrated in Fig. 6, the laser is focused on the Hf thin-film surface. Thus, the focused laser beam is first transmitted through the backside of the IR-FS and then strikes the Hf thin-film surface layer. The laser is operated in either a continuous wave or pulsed mode. The pulsed mode is according to a square wave, where a function generator is used to control the frequency, amplitude, and duty-cycle of the laser heating source. To regulate the laser heating area, a set of focusing lenses are used. In addition, a photodetector is used to monitor the laser heating performance via time-series detection of the reflected light from the Hf surface layer during jet-impingement cooling. Both 400-1000 nm reflectometry and laser diode reflectivity measurements show that the Hf thin-film has a reflectivity of  $\sim$  44% at 445 nm. Additionally, the internal transmissivity of the fused silica substrate at 445 nm was found to be > 0.97. This configuration facilitates the practical situation in microelectronics and other applications with nonuniform and highly local heat flux distributions instead of the usual uniformly heated plates.

To record a spatiotemporal evolution of temperature profile at the Hf thin-film surface, a FLIR SC7650 IR-camera (spectral sensitivity:  $1.5–5~\mu m$ , frame rate: 603 frames-per-second (fps), window size:  $160~\times~128$  pixels, pixel size:  $15.1~\mu m$ ) is used. Calibration of the IR-camera is done by a K-type thermocouple and by the procedure provided by the IR-camera manufacturer for evaluating the emissivity of the Hf thin-film layer and the transmissivity of the IR-FS substrate [42]. The global emissivity of the Hf thin-film on the IR-FS substrate is found to be  $\sim 0.6$ . This global emissivity within the FLIR IR camera spectral range of  $1.5–5~\mu m$  entails both the emissivity of the Hf thin-film and transmissivity of the IR-FS substrate. Fig. 6c presents the comparison between the Hf thin-film surface temperature measured by a thermocouple in contact with the surface of

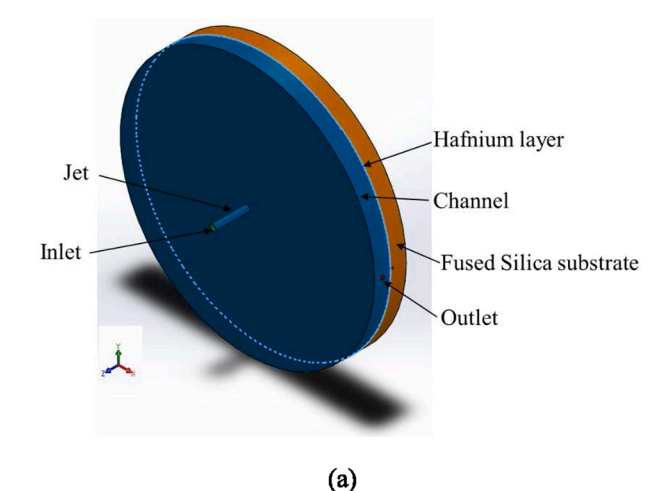
the Hf thin-film. The uncertainty of the IR temperature measurement is within  $\pm 0.2\text{--}0.6$  K when the surface temperature is below 40  $^{\circ}\text{C}$ , whereas the uncertainty rises to  $\pm 1\text{--}2$  K when the surface temperature is above 45  $^{\circ}\text{C}$ .

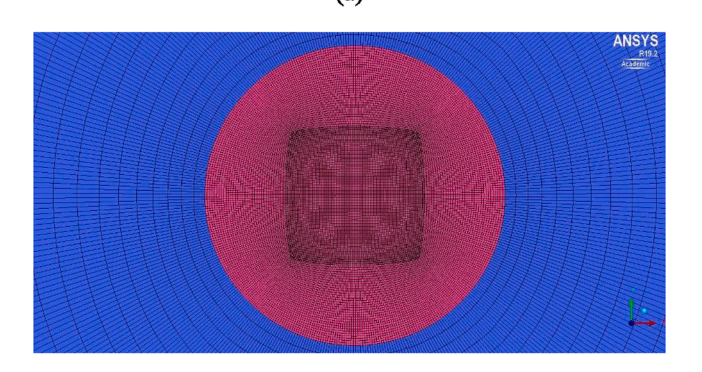
During the experiments, IR thermography images of the temperature around the hotspot were taken. Then, the edge detection method of Canny [43] was implemented to segment the hotspot region-of-interest (ROI). Snapshot IR camera images are also provided in Fig. 6 to illustrate the spatiotemporal evolution of the hotspot during submerged jet impingement cooling. The snapshot images correspond to one-half the laser heating cycle for square-wave heating at 75 Hz. The Supplemental Video provides the additional IR camera images for this same jet cooling experiment. For subsequent analysis of the IR temperature data, each temporal IR thermography frame is converted to an area-average ROI temperature. In this investigation, the results of the following operating conditions are reported: actual heat flux input of  $q^{**}=181~{\rm W/cm}^2$  (accounting for reflected power losses), heating frequency of  $f=75~{\rm Hz}$ , duty cycle of 50%, and the jet Reynolds number of Re = 2,000 (based on the jet diameter).

# 3.2. Numerical model

To predict the thermal behavior of the jet cooling system, a 3D numerical model was developed using commercial software ANSYS Fluent® [44], based on a careful reconstruction of the experimental device. Fig. 7a presents the geometry model which consists of a fused-silica (FS) substrate, round jet orifice of 1.2 mm in diameter and the channel through which the working fluid flows. The fluid enters via an orifice; the pipe length is 10 mm and then the jet is discharged into the round fluid chamber ( $\varnothing = 50.8$  mm). The jet strikes the chamber lower wall, coated by a 100 nm thick Hf thin-film, and finally the liquid exits through two square outlets located diametrically at both sides of the chamber. The properties of the materials involved are taken from the literature and are considered constant during the simulations, they are listed in Table 1.

A conjugate heat transfer problem was solved for the entire model, where convection modeling in the liquid was combined with conduction in all solid parts. The Hf thin-film was modeled using shell conduction, a





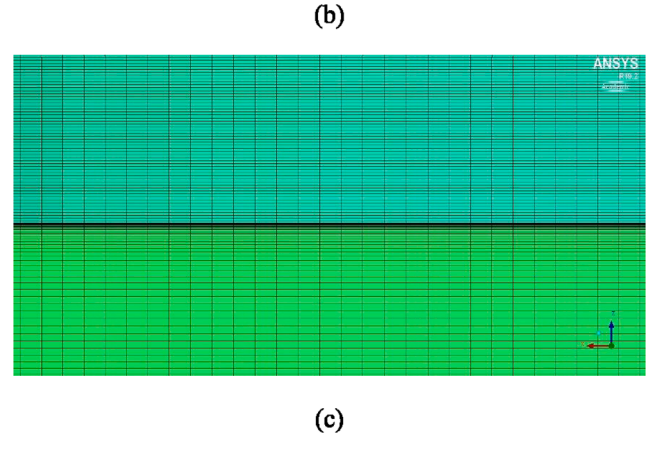


**Fig. 7.** Numerical schematics: (a) geometry model (not to scale for Hf), (b) grid structure of the jet in top view, (c) grid structure near the impingement surface (seen as a thick dark line).

**Table 1**Material thermal properties.

Material	Density kg·m <sup>-3</sup>	Specific heat J⋅kg <sup>-1</sup> ⋅K <sup>-1</sup>	Thermal conductivity $W \cdot m^{-1} \cdot K^{-1}$	Viscosity kg·m <sup>-1</sup> ·s <sup>-1</sup>
Liquid water	998.2	4,182	0.6	0.001
Fused silica	2,200	740	1.38	-
Hf	13,200	140	23	_

method incorporated in ANSYS Fluent which is very useful for applications where conduction in the plane of a thin wall is important. Instead of meshing the Hf thin-film (thickness of 100 nm), the software generates a 2D mesh in the wall plane with the prescribed thickness. The shell zone is coupled to the jet flow and to the FS substrate, and a 2D

energy equation is solved for it. In addition, to model the heat input from the laser, local volumetric heat generation rate, equivalent to the heating power, is assumed in the shell conduction zone. The thermal boundary conditions for all outer solid walls were insulation, while the temperature of the working fluid was assumed to be uniform at the entrance. The governing equation in the solid zone is the transient heat conduction equation:

$$\rho c_p \frac{\partial T}{\partial t} = \nabla \cdot (k \nabla T) + \dot{q}(\mathbf{x}) \tag{10}$$

where  $\dot{q}(\mathbf{x})$  is the local heat generation rate. The laser heating was modeled using a user defined function (UDF) code for the following variables: S – laser beam circular area, f – laser heating frequency, P – laser applied power. The heating was modeled using a uniform volumetric heat generation rate for the Hf thin-film at prescribed volume (according to S and height of 100 nm); the laser heated volume and jet center line were aligned with each other (at the line where x = y = 0).

As mentioned above, the properties of the water jet flow are considered constant, hence the jet flow is considered steady-state. Regarding the Reynolds number involved in this investigation ( $\approx$  2,000) and the authors' previous works [45,46], the flow region is not conclusively turbulent or laminar, thus the jet flow was modeled using both laminar and turbulent models. For the laminar cases, the convection was modeled using a basic set of three-dimensional continuity, momentum and energy equations:

$$\nabla \cdot \boldsymbol{u} = 0 \tag{11}$$

$$\frac{\partial \mathbf{u}}{\partial t} + (\mathbf{u} \cdot \nabla)(\mathbf{u}) = \frac{1}{\rho} \nabla p + \nu \nabla \cdot (\nabla \mathbf{u})$$
(12)

$$\rho c_p \frac{\partial T}{\partial t} + \rho c_p \mathbf{u} \cdot \nabla T = \nabla \cdot (k \nabla T)$$
(13)

For the turbulent case, the well-documented standard k- $\varepsilon$  model with enhanced wall treatment [47] is used to solve the jet. The equations of the standard k- $\varepsilon$  model are excluded herein since they are cumbersome and no specific contribution to their standard formulations was made during the present study. The model setup was made according to the default parameters suggested by ANSYS Fluent [44]. The flow boundary conditions were uniform velocity at the inlet orifice and pressure outlet at both system's outlets. No-slip and no penetration condition were used for all solid walls.

First, the flow field was solved using a steady-state solver, the energy equation is disabled for this initial stage. Once the steady flow field have converged, the energy equation was enabled and the transient solver was activated. The difference between the laminar and turbulent cases was found to be very small, e.g. 1.7 K at the stagnation point for constant heating (laser applied power P=0.15 W, laser circular area S=0.083 mm²) and Re = 2,000 at steady-state. We note that based on our previous experience, see Ref. [25], it was decided that the results presented in the results and discussion section below are the ones of the turbulent case.

The numerical scheme used to solve the flow field is basically the same as outlined in much detail in the authors' previous works, e.g. [25,46]. The computational grid was built using only hexahedral cells for the entire domain. Fig. 7b and 7c show top view of the jet inlet (colored in pink) and grid density at the impingement surface, respectively. The total number of computational cells in the final grid was 7,481,232. The methodology of mesh refinement is the same as described in much detail in our previous work, see Ref. [25]. Mesh refinement was employed in the jet inlet region and adjacent to the impingement region until changes in the results were negligible and a grid-independent solution was obtained. Like in Ref. [25], local velocity trends were examined along representative lines instead of an overall parameter, like the Nusselt number or pressure drop, which might be affected by various factors at different locations. Special care is given to

the near-wall grid resolution, so it is sufficiently fine. The enhanced wall treatment requires that the distance between the wall and the nearest node would be  $y^+$  equals to unity. The grid was designed carefully to fulfill this condition, as can be seen in Fig. 7c, which depicts the grid structure near the Hf thin-layer. A further in-depth discussion is given in Ref. [25].

Spatial discretization was done via second-order upwind scheme for momentum, energy and turbulence scalar equations. Semi-Implicit Method for Pressure Linked Equations (SIMPLE) was used for pressure–velocity coupling. A strict convergence condition was set,  $10^{-9}$  for the energy equation and  $10^{-6}$  for all the other conservation equations.

#### 3.3. Results and discussion

Flow characterization. As stated above, the water properties were taken as constant in the numerical simulation, therefore the jet flow field is in steady-state, even though the heat transfer problem is time-dependent. Fig. 8a and 8b present the simulated velocity contour and vector map, respectively, for jet Reynolds number of 2,000. From the figures, one can see the different jet flow regions as described in Ref. [48]. As expected, the stagnation region is aligned with the jet axis and stretches up to about the jet radius, then the fluid is forced to accelerate parallel to the impingement surface at the wall jet region. Since in our case the hotspot radius is in order of 10<sup>-4</sup> m and the jet radius is in order of 10<sup>-3</sup> m, regarding the jet flow regions the heat transfer is confined only to the stagnation zone.

Temperature distribution and heat transfer. The transient temporal temperature profile at the stagnation point, for simulated 75 Hz pulsed heating against the experimental data, is shown in Fig. 9. The temporal

data in Fig. 9 represents 10 heating cycles and illustrates how the Hf thin-film rapidly approaches a steady-periodic state. The corresponding Supplemental Video provides the spatiotemporal temperature data measured by IR thermography for an additional 30 heating cycles (40 total). In Fig. 9 the average hotspot temperature at the stagnation point is plotted for both the experiment and simulation with a water inlet temperature of 24 °C. We note that for the case of constant heating, the steady-state hotspot temperature reaches 62 °C. However, for this case of pulsed heating at  $f=75\,\mathrm{Hz}$  with the same nominal applied heat flux of  $q''=181\,\mathrm{W/cm^2}$ , the pulsed temperature profile's maximum and minimum peaks are rapidly stabilized at 57 °C and 31 °C, respectively. The temperature profile is characterized by sharp peaks since the transient thermal reaction does not reach the constant-heating steady state temperature when heating is done at  $f=75\,\mathrm{Hz}$ .

A normalized cycle can be calculated according to the following:  $\tilde{\tau}=ft-\mathrm{floor}(ft)$  where "floor" is a MATLAB function which rounds the argument to the closest integer toward negative infinity;  $\tilde{\tau}$  represents the relative location of the temperature sample in the cycle and its values are between 0 and 1. Once the system reached steady-periodic state ( $\tau>10$ ), the temporal temperature profiles for points on the line x=y=0, with different depth inside the FS substrate (for this system, the depth is y=-z), were plotted together in Fig. 10a for 0 to 100  $\mu$ m and in Fig. 10b for 100  $\mu$ m to 150  $\mu$ m (the figures are split for convenience and the depth of 100  $\mu$ m is included in both for reference). Like in the results of the analytical solution presented in Fig. 3, there are growing decay in the amplitude and delay in the phase of the temperature profile for greater depths. However, the simulated results do not show a constant mean temperature for all the different depths. To compare the analytical results with the numerical results, the penetration depth was calculated.

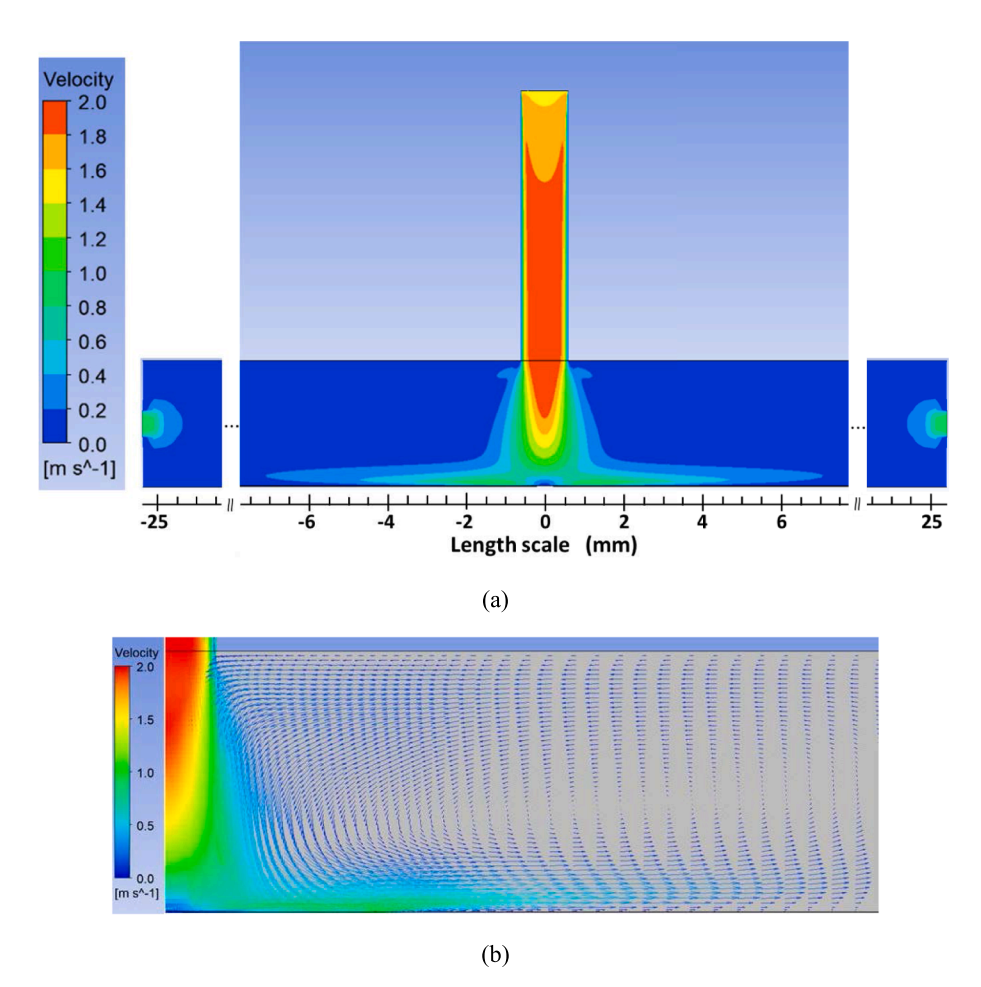


Fig. 8. The velocity field at the plane where y = 0 for Re = 2,000: (a) velocity magnitude contour, (b) velocity vector map.

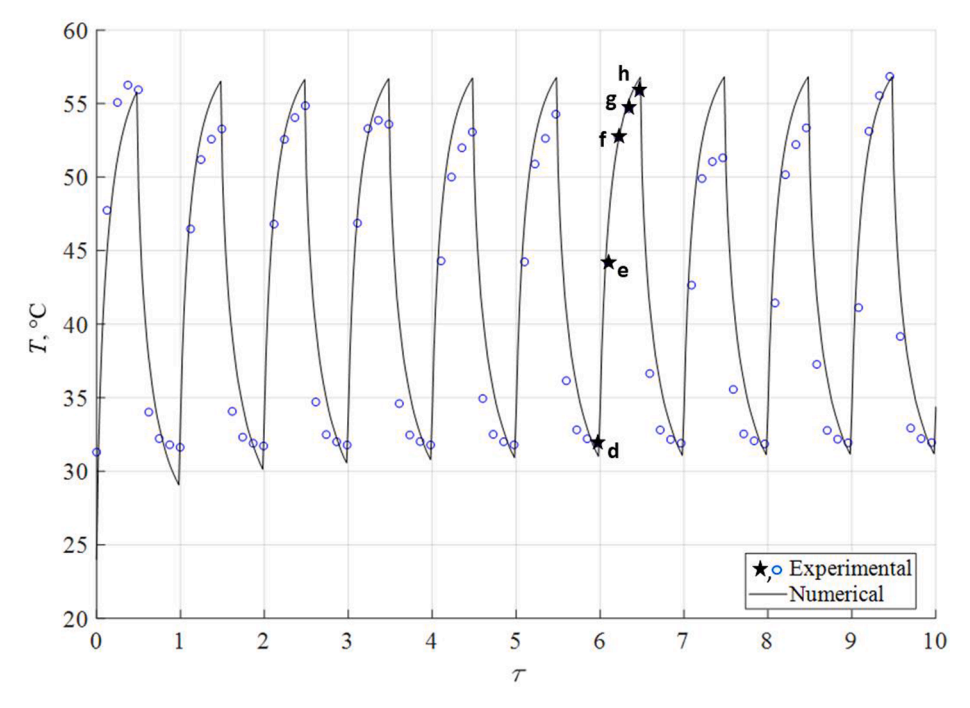


Fig. 9. Temporal temperature profile comparison between experimental and numerical results for  $q'' = 181 \text{ W/cm}^2$ , Re = 2,000, f = 75 Hz and duty cycle of 50%. For reference, the star symbols correspond to the snapshot IR camera images in Fig. 6d-h, where the Supplemental Video provides additional spatiotemporal IR camera data for this modulated hotspot heating experiment.

Analytically, the solution was performed again with the same properties of the system (material – FS, l=3.175 mm, f=75 Hz,  $\varphi=0$ ). For the numerical prediction, the amplitude was calculated for each depth in respect to its own mean temperature, and the amplitude was divided by the amplitude of the stagnation point. The comparison is plotted in Fig. 11. Although the boundary conditions are different, both the analytical slab and the simulated substrate excitations penetrate to the same depth (absolute difference of 0.05  $\mu$ m).

Since the jet flow is in steady-state, the heat transfer coefficient distribution is also temporally constant. In order to analyze the spatial distribution of the heat transfer coefficient and the Nusselt number, the temperature and heat-flux spatial distributions of the Hf thin-film are examined first. It was decided to present the contours for  $\tilde{\tau}=0.5$  at the peak of the temperature temporal profile. Fig. 12a shows an example of experimentally observed temperature contour of the Hf thin-film for steady heating with an applied hotspot heat flux of  $q^{\prime\prime}=181~{\rm W/cm^2}$ . Fig. 12b presents the numerical results when the hot-spot temperature is at its maximum. As expected, the highest temperature is in the area in which the laser is striking the Hf thin-film. The figure reveals that there is a planar heat spreading through the heated layer.

The heat flux distribution on the surface is affected by the jet flow, the heating profile and lateral conduction. Fig. 12c illustrates the wall heat flux distribution at the Hf thin-film. The heat flux into water is normalized by the nominal applied heat flux, which is 181 W/cm². Thus, the maximum value of the normalized flux (corresponding to the temperature peaks of Fig. 9,  $\tilde{\tau}=0.5$ ) is 0.77. This is because the lateral conduction in the Hf thin-film is significant.

Since the heat flux and the temperature contours exhibit axisymmetric distribution, they are plotted together in Fig. 13a at the line z=y=0 for  $0 \le x \le 500$  µm (for this case x is equivalent to the system's radial coordinate), in order to study the temperature and corresponding heat fluxes more closely. In the figure, the laser radius ( $\approx 160$  µm) is also presented. As it can be seen, the system has sharp decrease in temperature and heat flux values outside the hot spot area. For x>260 µm the heat flux values are becoming negative, which means that heat is transferred from the liquid into the Hf thin-film since there is a thin layer of liquid water with temperature higher than the Hf thin-film. The

minimum value of the heat flux is about  $6,000 \text{ W/m}^2$ , which is 0.3% of the nominal heat flux.

The heat transfer coefficient and the corresponding Nusselt number were calculated according to Newton's law of cooling, jet diameter and water properties. Since the Nusselt number and the heat transfer coefficient have the same profile, being different in their scales only, they are presented together in Fig. 13b. The maximum Nusselt number is 81 at the stagnation point (x=0); there is almost no change in the Nusselt number values up until  $x=150~\mu m$ , and then there is a sharp decrease in its value. After exiting the hotspot area, the Nusselt number keeps decreasing. There is a small zone with no convective heat transfer. Then, the heat transfer changes its direction, and the water heats the Hf thin-film

The findings discussed above allow for an additional validation of the present results. Sun et al. [41] conducted experimental study to disclose the local heat transfer characteristics of impinging submerged circular water jets. They derived the following correlation for the stagnation Nusselt number:

$$Nu = 1.02 \text{ Re}^{0.5} Pr^{0.368}$$
 (14)

According to their experimental conditions, the correlation was established for Re =5,000-36,000. Though it is above the present range, a comparison is of interest. Fluid properties were taken at film temperature by averaging the wall and fluid inlet temperature. To assess the numerical simulation results, the correlation was used for the studied case, Re =2,000, with film temperature of 41  $^{\circ}\text{C}$  resulting in Pr =4.04, yielding the correlated Nusselt number of 76.3. The Nusselt number obtained for the numerical prediction is Nu =81, which is within 6% of literature value.

# 4. Conclusion

This study has experimentally and numerically investigated the spatiotemporal heat transfer associated with periodic excitation in micro-scale systems. The study has explored the theoretical background concerning transient and periodic conduction problems to derive analytical solutions for a unidirectional case. Then, the analytical

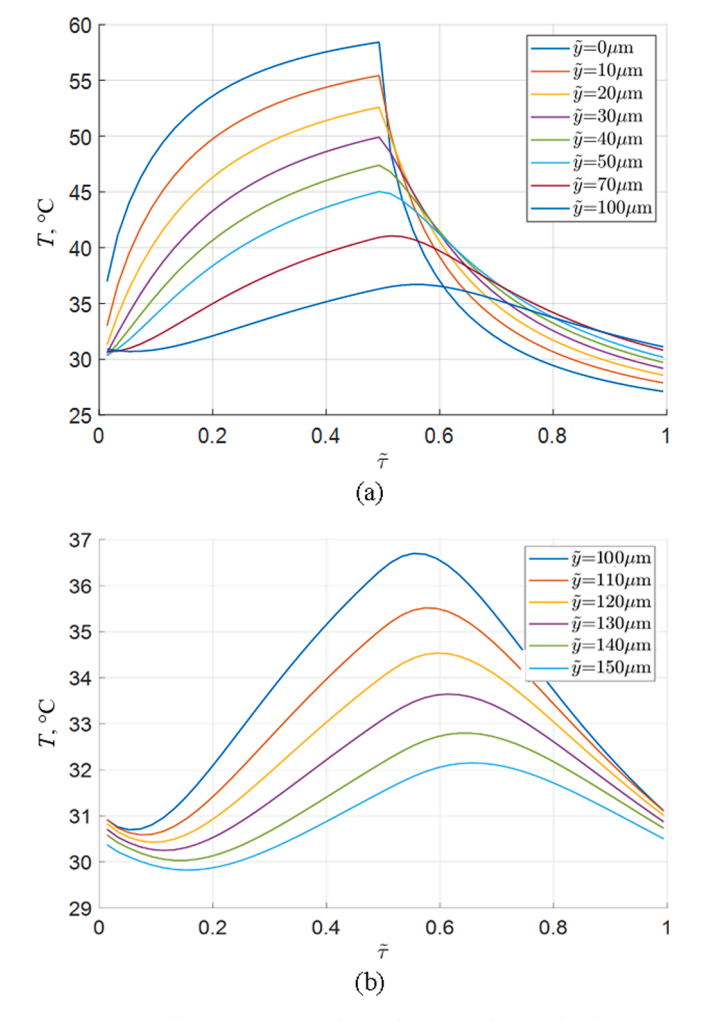


Fig. 10. Temporal temperature profile for different substrate depths: (a) 0 to 100  $\mu m,$  (b) from 100  $\mu m$  to 150  $\mu m.$ 

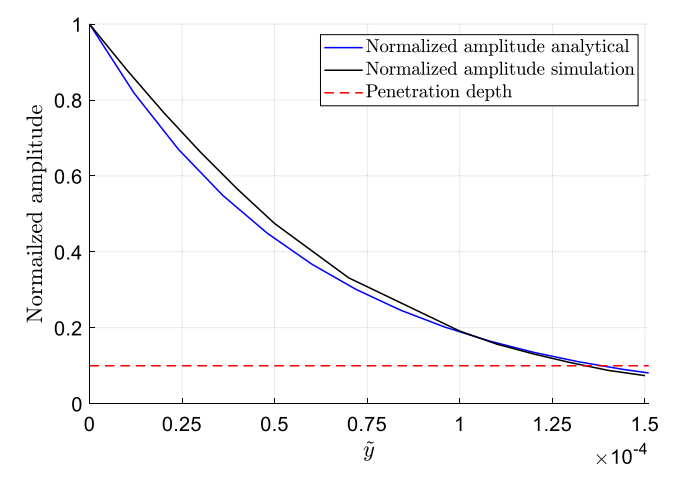
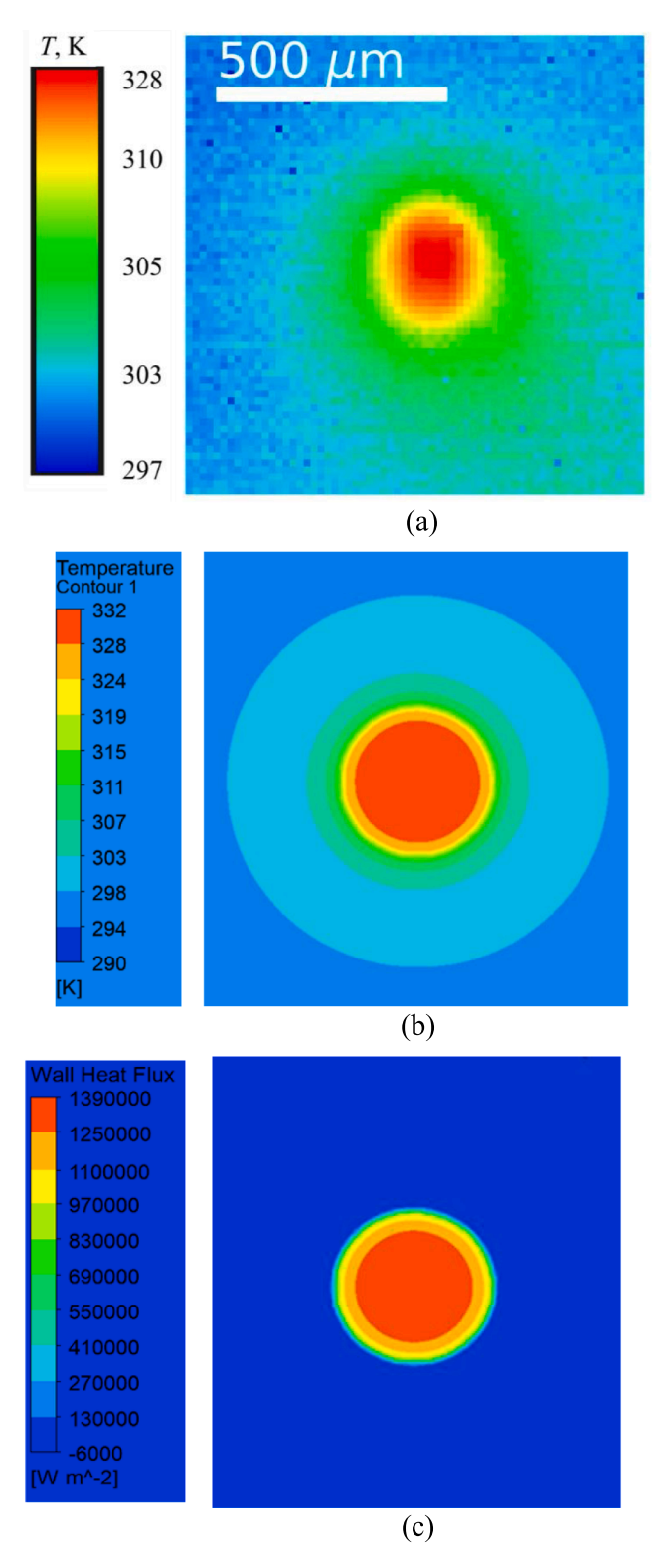


Fig. 11. Normalized amplitude analytical results and the experimental system simulation results.

solutions have been used to perform a parametric study on the penetration depth, a parameter which indicates the distance from the boundary at which the excitation is still noticeable.

As a demonstration, an experimental apparatus in which a surface is heated locally by a pulsing laser and is cooled by a steady liquid impinging jet, was examined. The system was numerically modeled and



**Fig. 12.** Hf thin-film data at  $\tilde{\tau}=0.5$ , comparison of the temperature contours shape of (a) experimental results, (b) numerical results, and (c) numerical heat flux contour. All images are at the same scale.

compared with the experimental temporal temperature profile to validate the numerical model. The numerical prediction was then used to characterize the relevant length and time scales. The three-dimensional numerical simulation elucidated the number of cycles the system undergoes till steady-periodic state is reached. The heat transfer coefficient and corresponding Nusselt number were calculated accordingly. To

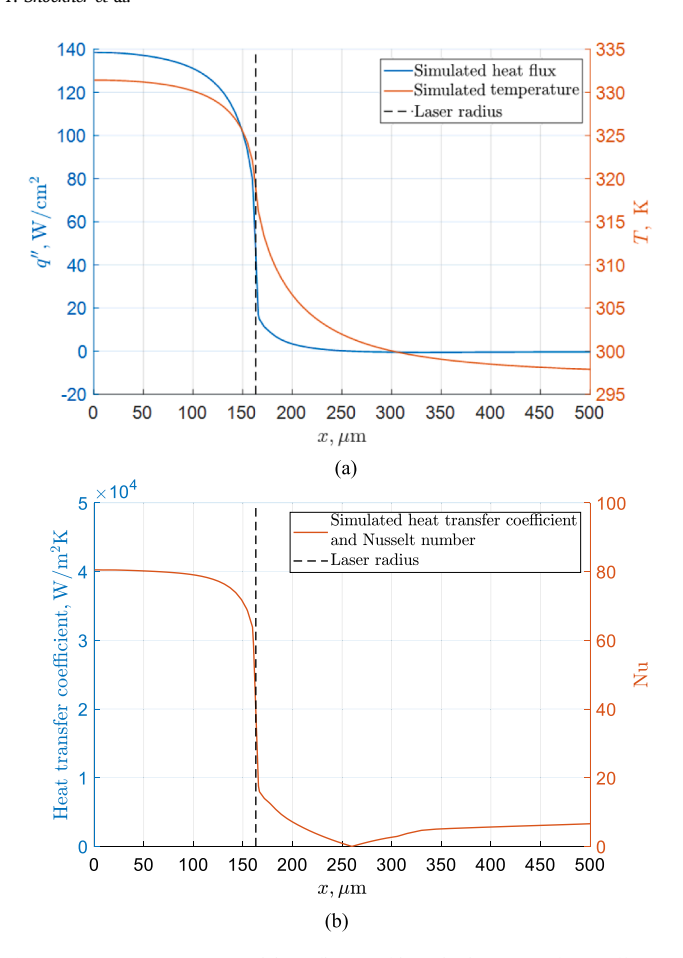


**Fig. 13.** (a) Temperature and heat-flux profiles, (b) heat transfer coefficient and Nusselt number profiles for different x locations on the line where y=z=0.

further assess the method of simulation, the numerically found stagnation Nusselt number was compared to a known correlation from the literature and was found to be practically the same.

The numerical predictions were also qualitatively compared with the analytical solutions for penetration depth, and a good agreement was found. The insights gained from this study can assist the design of systems with unsteady (in time) and nonuniform (in space) heating characteristics. A possible future direction of this study is understanding of more complex physically-driven transient phenomena in which a quasiperiodic behavior would be the result of a physical mechanism, which can alter the heat transfer coefficient temporarily, like boiling flow in micro-systems.

# **Declaration of Competing Interest**

The authors declare that they have no known competing financial interests or personal relationships that could have appeared to influence the work reported in this paper.

## Acknowledgments

This paper is based on research sponsored by the U.S. - Israel Binational Science Foundation (BSF) under Grant No. 2016399. The authors also acknowledge the experimental assistance by Chance Brewer, partially supported by UCF's undergraduate research F-LEARN program.

# Appendix A. Supplementary data

Supplementary data to this article can be found online at https://doi.

org/10.1016/j.applthermaleng.2021.117225.

#### References

- L.P. Yarin, A. Mosyak, G. Hetsroni, Fluid flow, heat transfer and boiling in microchannels, Springer, Berlin, 2009.
- [2] A.J. Robinson, Thermal-hydraulic comparison of liquid microchannel and impinging liquid jet array heat sinks for high-power electronics cooling, IEEE Trans. Compon. Packag. Technol. 32 (2) (2009) 347–357.
- [3] J. Mohammadpour, M. Rajabi-Zargarabadi, A.S. Mujumdar, H. Ahmadi, Effect of intermittent and sinusoidal pulsed flows on impingement heat transfer from a concave surface, Int. J. Thermal Sciences 76 (2014) 118–127.
- [4] A.H. Gitan, R. Zulkifli, S. Abdullah, K. Sopian, Development of pulsating twin jets mechanism for mixing flow heat transfer analysis, The Scientific World Journal 767614 (2014).
- [5] T. Persoons, A. McGuinn, D.B. Murray, A general correlation for the stagnation point Nusselt number of an axisymmetric impinging synthetic jet, Int. J. Heat Mass Tran. 54 (2011) 3900–3908.
- [6] T. Persoons, K. Balgazin, K. Brown, D.B. Murray, Scaling of convective heat transfer enhancement due to flow pulsation in an axisymmetric impinging jet, J. Heat Tran. 135 (2013), 111012.
- [7] T. Persoons, T. Saenen, T.V. Oevelen, M. Baelmans, Effect of flow pulsation on the heat transfer performance of a minichannel heat sink, J. Heat Tran. 134 (2012), 201723.
- [8] D. Klein, G. Hetsroni, Enhancement of heat transfer coefficients by actuation against an impinging jet, Int. J. Heat Mass Transf. 55 (2012) 4183–4194.
- [9] E. Sourtiji, Y. Peles, A micro-synthetic jet in a microchannel using bubble growth and collapse, Appl. Therm. Eng. 160 (2019), 114084.
- [10] Y.H. Liu, S.Y. Tsai, C.C. Wang, Effect of driven frequency on flow and heat transfer of an impinging synthetic air jet, Appl. Therm. Eng. 75 (2015) 289–297.
- [11] S.R. Rao, F. Houshmand, Y. Peles, Transient flow boiling heat-transfer measurements in microdomains. Int. J. Heat Mass Transf. 76 (2014) 317–329.
- [12] S. Bigham, S. Moghaddam, Microscale study of mechanisms of heat transfer during flow boiling in a microchannel, Int. J. Heat Mass Tran. 88 (2015) 111–121.
- [13] G. Wang, P. Cheng, An experimental study of flow boiling instability in a single microchannel, Int. Comm. in Heat and Mass Tran. 35 (10) (2008) 1229–1234.
- [14] T. Chen, S.V. Garimella, Measurements and high-speed visualizations of flow boiling of a dielectric fluid in a silicon microchannel heat sink, Int. J. Multiph. Flow 32 (8) (2006) 957–971.
- [15] A.K. Sadaghiani, N.S. Saadi, S.S. Parapari, T. Karabacak, M. Keskinoz, A. Kosar, Boiling heat transfer performance enhancement using micro and nano structured surfaces for high heat flux electronics cooling systems, Appl. Therm. Eng. 127 (2017) 484–498.
- [16] F. Yang, W. Li, X. Dai, C. Li, Flow boiling heat transfer of HFE-7000 in nanowire-coated microchannels, Appl. Therm. Eng. 93 (2016) 260–268.
- [17] E. Browne, M.K. Jensen, Y. Peles, Microjet array flow boiling with R134a and the effect of dissolved nitrogen, Int. J. Heat Mass Tran. 55 (4) (2012) 825–833.
- [18] G.J. Michna, E.A. Browne, Y. Peles, M.K. Jensen, The effect of area ratio on microjet array heat transfer, Int. J. Heat Mass Tran. 54 (9–10) (2011) 1782–1790.
- [19] E.A. Browne, G.J. Michna, M.K. Jensen, Y. Peles, Microjet array single-phase and flow boiling heat transfer with R134a, Int. J. Heat Mass Tran. 53 (23–24) (2010) 5072–5034
- [20] E.A. Browne, G.J. Michna, M.K. Jensen, Y. Peles, Experimental investigation of single-phase microjet array heat transfer, J. Heat Transfer 132 (4) (2010), 041013.
- [21] M.K. Sung, I. Mudawar, Single-phase hybrid micro-channel/micro-jet impingement cooling, Int. J. Heat Mass Tran. 51 (2008) 4342–4352.
- [22] Y. Zhuang, C.F. Ma, M. Qin, Experimental study on local heat transfer with liquid impingement flow in two-dimensional micro-channels, Int. J. Heat Mass Tran. 40 (17) (1997) 4055–4059.
- [23] J. Barrau, D. Chemisana, J. Rosell, L. Tadrist, M. Ibañez, An experimental study of a new hybrid jet impingement/micro-channel cooling scheme, Appl. Therm. Eng. 30 (2010) 2058–2066.
- [24] X.H. Yang, S.C. Tan, Y.J. Ding, J. Liu, Flow and thermal modeling and optimization of micro/mini-channel heat sink, Appl. Therm. Eng. 171 (2020), 115063.
- [25] J.H. Shin, T. Rozenfeld, T. Shockner, A. Vutha, Y. Wang, G. Ziskind, Y. Peles, Local heat transfer under an array of micro jet impingement using HFE-7000, Appl. Therm. Eng. 158 (2019), 113716.
- [26] R.G. Nevins, H.D. Ball, Heat transfer between a flat plate and a pulsating impinging jet, Proceedings of the National Heat Transfer Conference 60 (1961) 510–516.
- [27] H.S. Sheriff, D.A. Zumbrunnen, Effect of flow pulsations on the cooling effectiveness of an impinging jet, J. Heat Tran. 116 (4) (1994) 886–895
- [28] E.C. Mladin, D.A. Zumbrunnen, Local convective heat transfer to submerged pulsed jets, Int. J. Heat Mass Tran. 40 (1997) 3305–3321.
- [29] D.J. Sailor, D.J. Rohli, Q. Fu, Effect of variable duty cycle flow pulsations on heat transfer enhancement for an impinging air jet, Int. J. Heat Fluid Flow 20 (1999) 574-580
- [30] E.C. Mladin, D.A. Zumbrunnen, Alterations to coherent flow structures and heat transfer due to pulsations in an impinging air-jet, Int. J. Therm. Sci. 39 (2000) 236–248
- [31] W. Zhou, L. Yuan, X. Wen, Y. Liu, D. Peng, Enhanced impingement cooling of a circular jet using a piezoelectric fan, App. Therm. Eng. 160 (2019), 114067.
- [32] G. Ziskind, L.P. Yarin, S. Peles, C. Gutfinger, Experimental investigation of particle removal from surfaces by pulsed air jets, Aerosol Sci. Technol. 36 (2002) 652–659.
- [33] Carslaw, H.S., Jaeger, J.C., Conduction of Heat in Solids, 2nd ed., Oxford University Press, London, 1959.

- [34] Jakob, M., Heat Transfer, Volume I, 5th ed., John Wiley & Sons, Inc., New York, 1956.
- [35] Arpaci, V.S., Conduction Heat Transfer, Addison-Wesley, USA, 1966.
- [36] Kakac, S., Yener, Y., Naveira-Cotta, C.P., Heat Conduction, 5th ed. CRC press, 2018.
- [37] Hahn, D.W., Ozisik, M.N., Heat Conduction, 3rd ed., John Wiley & Sons, Inc., 2012.
- [38] J. Khedari, P. Benigni, J. Rogez, J.C. Mathieu, A solution of the heat conduction equation in the finite cylinder exposed to periodic boundary conditions: the case of steady oscillation and constant thermal properties, Proc. R. Soc. Lond. A 438 (1992) 319–329.
- [39] MATLAB version 9.5.0.944444 (R2018b), Natick, Massachusetts: The MathWorks Inc
- [40] Batchelor, G.K., An Introduction to Fluid Dynamics, Cambridge University Press, 2000
- [41] H. Sun, C.-F. Ma, W. Nakayama, Local characteristics of convective heat transfer from simulated microelectronic chips to impinging submerged round water jets, J. Electron. Package. 115 (1993) 71–77.

- [42] R. Danjoux, Window and external optics transmittance, http://support.flir.com/ Answers/A817T/A817-T560472\_A-en-US%20Technical%20publication%2060% 20Window%20or%20External%20Optics%20Transmittance.pdf, accessed: December 2020.
- [43] Canny, J., A computational approach to edge detection, IEEE Transactions on Pattern Analysis and Machine Intelligence, PAMI-86, pp. 679-698, Nov. 1986.
- [44] ANSYS Fluent version 19.2.0, Canonsburg, Pennsylvania: ANSYS Inc.
- [45] A.K. Vutha, T. Rozenfeld, J.H. Shin, S. Rao, Y. Wang, G. Ziskind, Y. Peles, Spatial temperature resolution in single-phase micro slot jet impingement cooling, Int. J. Heat Mass Tran. 118 (2018) 720–733.
- [46] A. Gorodetsky, T. Rozenfeld, H.D. Haustein, G. Ziskind, Flow and heat transfer analysis of hybrid cooling schemes: Adding micro-jets to a micro-gap, Int. J. Thermal Sciences 138 (2019) 367–383.
- [47] S. Barboy, A. Rashkovan, G. Ziskind, Determination of hot spots on a heated wavy wall in channel flow, Int. J. Heat Mass Tran. 55 (2012) 3576–3581.
- [48] B.W. Webb, C.-F. Ma, Heat transfer characteristics of single-phase impinging liquid jets, Advances in Heat Transfer 26 (1995) 105–218.